that that model executed during the simulation. The field threading the inner core was at that time very weak, so that the magnetic torque Γ_B was small. Note also that our models (*1, 2*) have assumed phase equilibrium on the inner core boundary; that is, as thermodynamic conditions change, freezing and melting occurs instantaneously to maintain the boundary at the freezing point. No allowance has been made for a finite time of relaxation to such a state. If that relaxation time were long compared with the time scales of interest in our model, the inner core would behave as a solid. As B. A. Buffett [*Geophys. Res. Lett.* **23**, 2279 (1996)] noted, the orientation of the inner core would then plausibly be gravitationally "locked" to that of the mantle by the inner core topography created by mantle inhomogeneities, which we have not included in our models. If Earth's inner core is rotating faster than the mantle, as recent observations suggest (*9, 10*), a short melting-freezing relaxation time, a "mushy zone" at the top of the inner core (D. E. Loper, private communication), or a low inner core viscosity (B. A. Buffett, private communication) may preclude this gravitational locking effect.
9. X. Song and P. G. Richards, *Nature* **382**, 221 (1996).
10. W. Su, A. M. Dziewonski, R. Jeanloz, *Science* **274**, 1883 (1996).
11. R. Hollerbach and C. A. Jones, *Nature* **365**, 541(1993); *Phys. Earth Planet. Inter.* **87**, 171 (1993).
12. For example, P. H. Roberts [*Philos. Trans. R. Soc. London Ser. A* **263**, 93 (1968)] analyzed convection in a sphere, rapidly rotating as measured by the Taylor number *Ta*. He showed that the critical temperature gradient, as measured by a Rayleigh number *Ra*, at which convection could marginally occur is of order $Ta^{2/3}$ for both axisymmetric and nonaxisymmetric modes of convection, but that the nonaxisymmetric motions, later identified by F. H. Busse [*J. Fluid Mech.* **44**, 441 (1970)] as rolls parallel to the rotation axis, have the smaller critical *Ra*. That such rolls are "preferred" can be qualitatively understood in terms of the Proudman-Taylor theorem: Slow, steady motions in an inviscid rotating fluid are 2D with respect to the rotation axis, so that a towed body in such conditions carries a column of fluid with it, a so-called Taylor column. The convective rolls are also often called, a little imprecisely, Taylor columns.
13. Similar thermal wind and meridional circulation structures were obtained by P. Olson and G. A. Glatzmaier [*Phys. Earth Planet. Inter.* **92**, 109 (1995)] using a fully 3D magnetoconvection model but with an imposed zonal magnetic field and a nonrotating, insulating inner core. Similar flow structures also have been obtained by C. Jones and R. Hollerbach (private communication) with their dynamo model using only one nonaxisymmetric mode.
14. Phrases like "just above the inner core boundary" are used in this discussion for presentational simplicity. The fluid in contact with the inner core boundary moves with it because of the no-slip boundary condition; there is no relative motion at the boundary. More precisely, the key quantities determining the coupling between inner and outer cores are B_r and the derivatives of **V** on the inner core boundary, which control B_ϕ and hence the stress $B_r B_\phi/\mu_0$ on the inner core boundary. Also, after writing this report we were given a preprint by J. Aurnou, D. Brito, and P. Olson (*Geophys. Res. Lett.*, in press) that describes a simple, analytic model of inner core rotation that approximates the thermal wind and magnetic coupling present in our geodynamo simulations (*1, 2*).
15. There is no generally accepted way of defining τ_{em}. We take $\tau_{em} = \mu_0 \sigma R^2/\pi^2$, where R is the Earth's inner core radius, which is appropriate for a sphere surrounded by an insulator. This gives $\tau_{em} \approx 2400$ years, which is large compared with typical time scales of the fluid motion. The magnetic fields emerging from the inner core impose time scales of order τ_{em} on the geodynamo mechanism and stabilize it against polarity reversals, a significant fact first suggested by Hollerbach and Jones (*11*) and confirmed by our simulations (*1, 2*). The absence of zonal field in an inner core coupled magnetically to a fluid core was noted by S. Braginsky [*Geomagn. Aeron.* **4**, 572 (1964)].
16. The viscous stress-free boundary condition forces $\partial\omega/\partial r$ to vanish on the inner core boundary, so the net viscous torque Γ_ν vanishes there (*7*). This zero torque results in discontinuities in the horizontal velocity between the solid inner core surface and the fluid just above it, which make nonlinear contributions to the magnetic boundary conditions there.
17. F. D. Stacey, *Physics of the Earth* (Brookfield, Brisbane, Australia, ed. 3, 1992).
18. The computing resources were provided by the Pittsburgh Supercomputing Center under grant MCA94P016P and the Advanced Computing Laboratory at Los Alamos National Laboratory. Different aspects of this work were supported by Los Alamos Laboratory Directed Research and Development grant 96149, University of California Directed Research and Development grant 9636, Institute of Geophysics and Planetary Physics grant 713 and NASA grant NCCS5-147. P.H.R. was supported by NSF grant EAR94-06002. The work was conducted under the auspices of the U.S. Department of Energy, supported (in part) by the University of California, for the conduct of discretionary research by Los Alamos National Laboratory.

13 August 1996; accepted 29 October 1996

Tomography of the Source Area of the 1995 Kobe Earthquake: Evidence for Fluids at the Hypocenter?

Dapeng Zhao*, Hiroo Kanamori, Hiroaki Negishi, Douglas Wiens

Seismic tomography revealed a low seismic velocity (−5%) and high Poisson's ratio (+6%) anomaly covering about 300 square kilometers at the hypocenter of the 17 January 1995, magnitude 7.2, Kobe earthquake in Japan. This anomaly may be due to an overpressurized, fluid-filled, fractured rock matrix that contributed to the initiation of the Kobe earthquake.

The 17 January 1995, magnitude (M) 7.2, Kobe (Hyogo-Ken Nanbu) earthquake was the most damaging earthquake to strike Japan since the Kanto earthquake in 1923 (*1*). The Kobe earthquake occurred in an area with complex structure including numerous active Quaternary faults that have produced many large historical earthquakes (*2*). The permanent seismic networks in southwestern Japan (*3*) and many portable stations deployed following the Kobe mainshock (*4*) recorded thousands of aftershocks, which provide arrival time and waveform data for the determination of detailed crustal structure in the source area of the Kobe earthquake. Some previous tomographic studies found that some earthquake nucleation zones showed higher velocities than the surrounding country rock. These high velocity zones may represent competent parts of the fault zones or may indicate regions of transition from stable to unstable sliding (*5*). Other studies found that nucleation zones had low velocities and a high Poisson's ratio (σ) that suggested the existence of overpressurized fluids (*6, 7*). We conducted an investigation of the seismic structure in the Kobe earthquake source area to understand what may have triggered this earthquake and how the rupture proceeded after initiation.

We used the tomographic method of Zhao *et al.* (*8*) to determine the three-dimensional (3D) *P*- and *S*-wave velocity (V_p, V_s) and σ distribution maps in the source area of the Kobe earthquake. We used 3203 Kobe aftershocks and 431 local micro-earthquakes that generated 64,337 *P*- and 49,200 *S*-wave arrival times (Fig. 1). Most of the events were located in and around the rupture zone of the Kobe earthquake [the zone extends about 130 km northeast from the southern part of Awaji Island to Lake Biwa (Fig. 1)]. All the events were recorded by more than 15 stations, and the hypocenter locations are accurate to ±1 to 2 km (*4, 9*). The data were recorded by 37 permanent stations (*3*) and 30 portable stations that were set up following the Kobe mainshock (Fig. 1B) (*4*). The picking accuracy of *P*- and *S*-wave arrival times is 0.05 to 0.15 s (*3, 4*).

Large V_p and V_s variations of up to 6% and σ variations of up to 10% were revealed in the Kobe rupture zone (Figs. 2 to 4). The tomographic inversions imaged the Kobe rupture zone as a low velocity zone from the surface to a depth of 20 km with a width of 5 to 10 km (Figs. 3 and 4) (*10*). On average, V_p and V_s in the fault zone were 3 to 4% lower than the surrounding country rock velocities. V_p was slower in the northeastern segment of the aftershock zone (the Suma and Suwayama faults) than that in the southwestern segment (the Nojima fault on Awaji Island) (Fig. 2A), while V_s was slower along the Nojima fault (Fig. 2B). Therefore the Suma and Suwayama

D. Zhao and D. Wiens, Department of Earth and Planetary Sciences, Washington University, St. Louis, MO 63130, USA.
H. Kanamori, Seismological Laboratory 252-21, California Institute of Technology, Pasadena, CA 91125, USA.
H. Negishi, Disaster Prevention Research Institute, Kyoto University, Uji 611, Japan.

*To whom correspondence should be addressed. E-mail: dapeng@izu.wustl.edu

faults exhibited smaller values of σ than the Nojima fault (Fig. 2C). The Nojima fault showed slow V_s and high σ to a depth of 5 km, which may be associated with the soft and thick alluvial sediments that have a high water content (*1, 11*). The V_s image is different from the V_p image, probably because *S* waves are more sensitive to the fluid content of the rock than are *P* waves (*12*).

There is a low V_p, low V_s, and high σ anomaly at the Kobe hypocenter at a depth of 16 to 21 km (Figs. 2 to 4) that extends laterally 15 to 20 km and covers about 300 km^2. To confirm that this anomaly was adequately resolved by the inversion, we conducted checkerboard resolution tests (*8, 13*) (Fig. 5). The resolution tests, with a grid spacing of 5 km, indicate good resolution for V_p and V_s anomalies along the Kobe fault zone (Fig. 5, B and D). For the tests with a grid spacing of 9 km, the resolution is good for areas within 20 km of the fault zone (Fig. 5, A and C). The shallower areas, to a depth of 18 km, showed the highest resolution (Fig. 5). We also examined the ray path coverage, particularly in and around the low velocities, high σ anomaly at the Kobe hypocenter. There were numerous rays crisscrossing that region from events outside the anomaly and events outside the cross section (Fig. 1, line A-B) to the stations in the epicentral area. We also conducted tomographic inversions and resolution tests with different grid spacing, initial velocity models, and different data sets. The results showed that the low velocities, high σ anomaly at the Kobe hypocenter could be resolved.

Seismic waves passing through the Nojima fault near the Kobe hypocenter exhibited strong attenuation (*14*). Shear wave splitting was observed along the Nojima fault (*15*). These observations suggest the presence of cracks, fluids, or both in the fault zone that could cause the attenuation and shear wave splitting. Ito *et al.* (*16*) suggested that the thickness of the seismogenic layer changes from about 13 km thick in the northeast (beneath the Suma and Suwayama fault traces) to about 17 km thick in the southwest (beneath the Nojima fault trace). There is a gap in the aftershock seismicity, just to the northeast of the mainshock hypocenter (Figs. 2 and 3), that was interpreted as dense, unfractured rock on the fault plane (*17*). The overall stress field in the Kobe region has the maximum compressional stress oriented east-west, but it was oriented north-south in the mainshock epicentral area (*18*). Reflected seismic waves were detected from seismograms of aftershocks beneath northern Awaji Island, with a duration of 2 to 3 s, implying that seismic reflectors were densely distributed beneath the hypocenter at depths of 20 to 30 km (*19*). These observations suggest structural heterogeneity in the Kobe hypocenter area.

Seismic velocity and Poisson's ratio in crustal rocks depend on factors such as temperature, pressure, composition, crack density, and fluid content. A few general properties have emerged from laboratory and in situ velocity experiments, though the relationships are not completely understood for all rock types. Low V_p, low V_s, and high σ may be associated with fluid-filled, fractured rock (*12*) or magma reservoirs (*8, 20*). Near Kobe there is no active volcano (*21*) (Fig. 1C), and heat flow studies revealed no significant lateral changes in temperature before the earthquake (*22*). Therefore we suggest that the anomaly at the Kobe hypocenter is not related

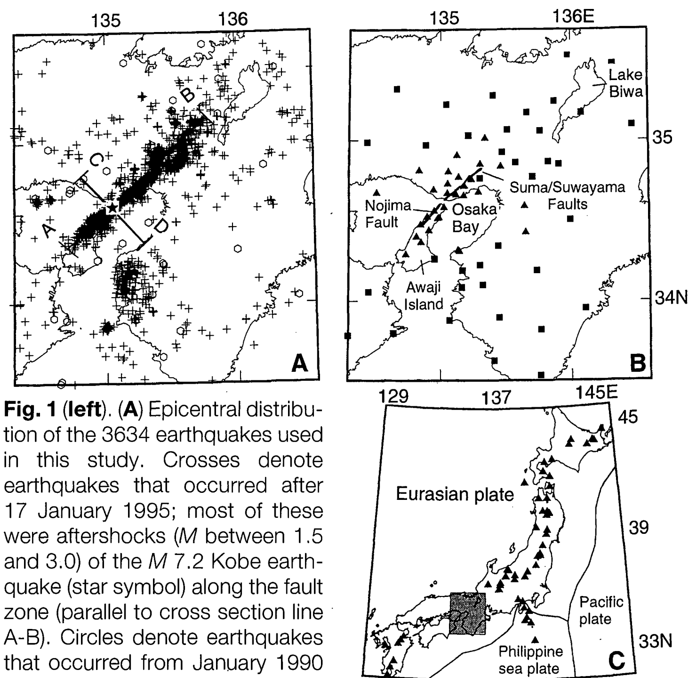

Fig. 1 (**left**). (**A**) Epicentral distribution of the 3634 earthquakes used in this study. Crosses denote earthquakes that occurred after 17 January 1995; most of these were aftershocks (*M* between 1.5 and 3.0) of the *M* 7.2 Kobe earthquake (star symbol) along the fault zone (parallel to cross section line A-B). Circles denote earthquakes that occurred from January 1990 to December 1994, with *M* between 1.8 and 4.0. Lines A-B and C-D show the locations of the cross sections in Figs. 2 and 3. (**B**) Distribution of seismic stations that recorded the earthquakes in (A). Solid triangles denote portable stations that were set up following the Kobe mainshock. Solid squares denote permanent stations. Solid lines represent the surface traces of the Nojima, Suma, and Suwayama faults. (**C**) The general tectonic setting of the Japan Islands. Curved thick lines show the major plate boundaries. Solid triangles denote active volcanoes. The shaded area shows the present study area in (A) and (B).

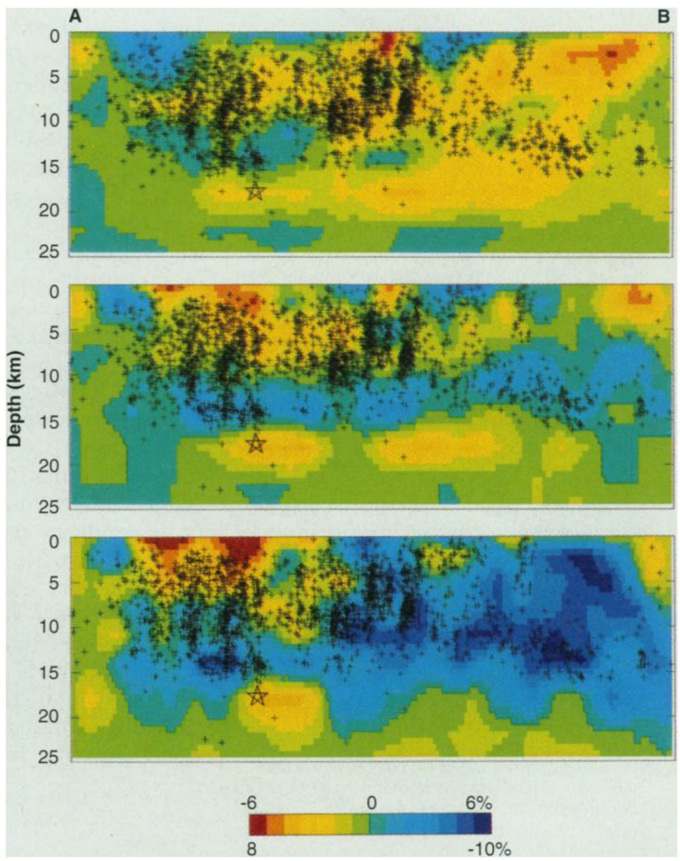

Fig. 2 (**right**). Vertical cross sections of V_p (**top**), V_s (**middle**), and σ (**bottom**) along the line A-B shown in Fig. 1A. Slow velocity and high σ ratio are shown in red; fast velocity and low σ ratio are shown in blue. V_p and V_s perturbations range from −6% to 6% from the one-dimensional velocity model. The σ ratio ranges from 0.225 to 0.27 (−10% to 8% from the average value). Small crosses denote the Kobe aftershocks within a 6-km width along the line A-B. The star symbol denotes the hypocenter of the Kobe mainshock; its focal depth is 17.7 km. The vertical exaggeration is 2:1.

to a magma reservoir, but rather to the presence of fluids in the crust. Lithological heterogeneity in the crust would also cause anomalies in V_p, V_s, and σ. However, it is difficult to explain all the observations for the Kobe hypocenter area (*14–19*) with lithological variation only. For example, strong seismic attenuation and local stress change may not happen due to a change in lithology at a depth of 18 km in the crust. Future investigations using other geophysical methods, such as magnetotelluric soundings, would provide further constraint on this interpretation (*7*).

The low velocities, high σ anomaly at the Kobe hypocenter may be due to overpressurized, fluid-filled, fractured rock matrix near the bottom of the seismogenic layer. Potential sources of the fluids may be dehydration of minerals, fluids trapped in pore spaces, and meteoric water (*23*). The subducting Philippine Sea plate is 50 to 60 km deep in this area (*24*). The subducted oceanic crust on the top of the slab may also contribute to the fluids in the crust. The existence of overpressurized fluids beneath the seismogenic layer may affect the long-term structural and compositional evolution of the fault zone, change the strength of the fault zone, and alter the local stress regime (*25*), as observed in the hypocentral area (*18*). These influences may have enhanced stress concentration in the seismogenic layer leading to mechanical failure, and thus may have contributed to the nucleation of the Kobe earthquake.

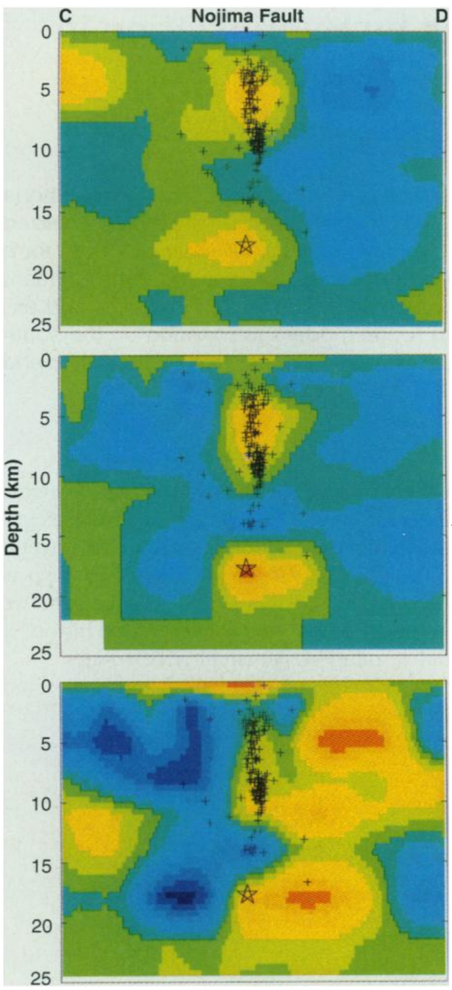

Fig. 3. Vertical cross sections of V_p (**top**), V_s (**middle**), and σ (**bottom**) along the line C-D shown in Fig. 1A. The Kobe aftershocks within a width of 6 km along the line C-D are plotted as crosses. Scale bar and labeling are as in Fig. 2.

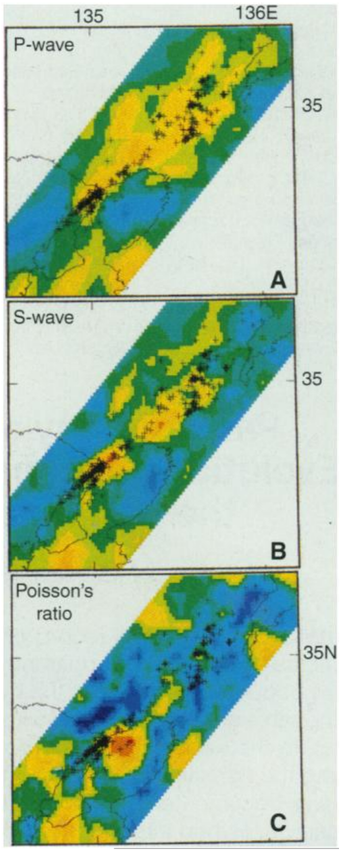

Fig. 4. Distribution of V_p (**A**), V_s (**B**), and σ (**C**) at a depth of 18 km. The Kobe aftershocks at a depth of 13 to 23 km are plotted as crosses. Scale bar and labeling are as in Fig. 2.

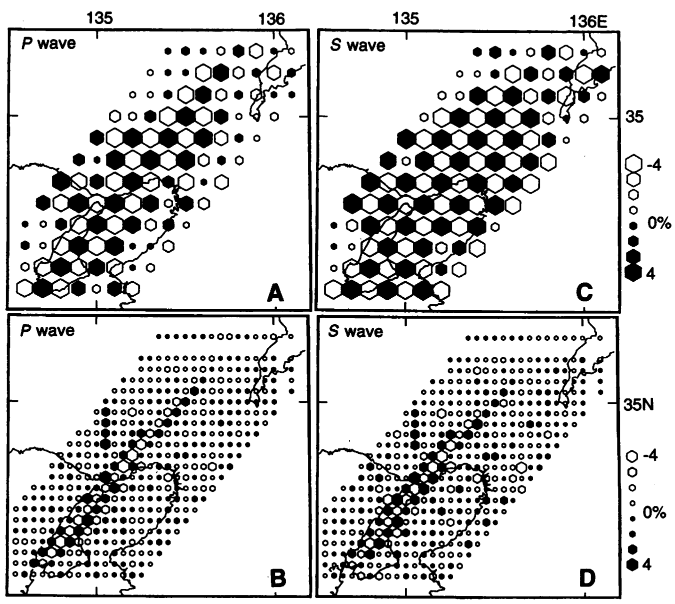

Fig. 5. Results of checkerboard resolution tests for V_p (**left**) and V_s (**right**) structures at a depth of 18 km. The grid spacing is 9 km in (**A**) and (**C**) and 5 km in (**B**) and (**D**). Open and solid circles denote low and high velocities, respectively. The perturbation scales are shown on the right.

REFERENCES AND NOTES

1. H. Kanamori, *Seismol. Res. Lett.* **66**, 6 (1995); P. Somerville, *Eos* **76**, 49 (1995).
2. T. Hagiwara, Ed., *Earthquakes in the Japan Islands: Seismotectonics and Structure* (Kashima Press, Tokyo, 1990). The Kobe epicenter is about 200 km north of the Nankai Trough (the major plate boundary between the Philippine Sea plate and the Eurasian plate, Fig. 1C), and about 40 km from the Median Tectonic Line, which is a large strike-slip fault zone in southwestern Japan. Numerous active Quaternary faults exist in the region. In the past century, four major intraplate earthquakes have occurred in central to western Japan: the 1891 Nobi (M = 8), 1927 Tango (M = 7.3), 1943 Tottori (M = 7.2), and 1948 Fukui (M = 7.1) earthquakes. Two historical earthquakes occurred in the vicinity of the Kobe earthquake, $M > 7$ in 868, and $M > 6$ in 1916.
3. S. Tsuboi *et al.*, *J. Seismol. Soc. Japan* **42**, 277 (1989). More than 90 permanent seismic stations are operated in southwestern Japan by Kyoto University, Nagoya University, Kochi University, Kyushu University, and the University of Tokyo, which are used to detect and record micro-earthquakes in this region. Among the 37 stations used in this study (Fig. 1B), 33 are equipped with three-component seismographs and four with one-component seismometers. All the *P*- and *S*-wave arrival times were double-checked by the analysts of the permanent networks.
4. S. Ohmi, *Progr. Abstr. Fall Meet. Seismol. Soc. Japan*, A39 (1995); Y. Umeda, *Proc. 1996 Japan Earth Planet. Sci. Meet.*, 36 (1996); N. Hirata and the Urgent Observation Group (GROUP-95) for the 1995 Hyogo-Ken Nanbu Earthquake, *J. Phys. Earth*, in press. All 30 portable stations are equipped with three-component seismometers. All the *P*- and *S*-wave arrival times were double-checked by the GROUP-95 analysts and the present authors. More than 98% of the *P*- and *S*-wave data used in this study was generated by the Kobe aftershocks and local micro-earthquakes with $M < 3$. The dominant frequency was 8 to 10 Hz for *P* waves and 5 to 8 Hz for *S* waves, and the Fresnel zones did not exceed 0.8 km, which is much smaller than the grid spacing

we adopted in this study.
5. J. M. Lees, *Geophys. Res. Lett.* **17**, 1433 (1990); J. M. Lees and C. E. Nicholson, *Geology* **21**, 387 (1993); W. Foxall, A. Michelini, T. V. McEvilly, *J. Geophys. Res.* **98**, 17691 (1993); D. Zhao and H. Kanamori, *Geophys. Res. Lett.* **20**, 1083 (1993); *ibid* **22**, 763 (1995).
6. D. Eberhart-Phillips and A. J. Michael, *J. Geophys. Res.* **98**, 15737 (1993); P. A. Johnson and T. V. McEvilly, *ibid.* **100**, 12937 (1995); G. S. Fuis *et al.*, *Eos* **77**, 173 (1996).
7. H. K. Gupta, S. V. S. Sarma, T. Harinarayana, G. Virupakshi, *Geophys. Res. Lett.* **23**, 1569 (1996). Seismologic and magnetotelluric studies revealed a low-velocity, high conductive anomaly near the hypocenter of the 1993 Latur earthquake in India. The anomaly was interpreted as a fluid-filled, fractured rock matrix that may have contributed to the nucleation of the Latur earthquake.
8. D. Zhao, A. Hasegawa, S. Horiuchi, *J. Geophys. Res.* **97**, 19909 (1992). We set up a 3D grid in the study area with a grid spacing of 4 to 5 km in the horizontal direction and 2 to 4 km in depth. Hypocenter locations and velocities at the grid nodes are taken as unknown parameters. The velocity at any point in the model is calculated by linearly interpolating the velocities at the eight grid nodes surrounding that point. An efficient 3D ray tracing technique is used to compute travel times and ray paths. We used a conjugate gradients algorithm to invert the large and sparse system of observation equations that relate the observed arrival-time data to the unknown parameters. *P*- and *S*-wave velocity structure and hypocenter parameters are simultaneously determined in an iterative inversion process. Then we use the relation $(V_P/V_S)^2 = 2(1 - \sigma)/(1 - 2\sigma)$, to determine σ distribution. The tomographic inversion was conducted for the area shown in Fig. 1. Only the ray paths within that area were used in the inversion. We did not use station corrections in our parameterization; any local anomalies close to stations can be resolved as velocity anomalies at the grid nodes of the top grid mesh layer at a depth of 0 km. Elevations of stations are included in the 3D ray tracing. The initial one-dimensional velocity model consists of four layers that are separated by the Conrad and Moho discontinuities and a velocity boundary at a depth of 3 km. In the four layers, V_p is 4.8, 6.0, 6.7, and 7.8 km/s. V_p/V_s ratio is 1.73. The Conrad discontinuity is at a depth of 15 to 17 km, and the Moho is at a depth of 34 to 35 km in the Kobe area (D. Zhao, S. Horiuchi, A. Hasegawa, *Tectonophysics* **212**, 289 (1992)). We have taken into account the Conrad and Moho depth changes in the tomographic inversions and found that the velocity changes due to the Conrad and Moho depth variations are less than 0.5% in the tomographic images (Figs. 2 through 4).
9. D. Zhao, H. Kanamori, D. Wiens, H. Negishi, *Eos (fall suppl.)* **76**, 378 (1995).
10. Fault zones are typically less than 1 km wide and composed of highly fractured material, fault gouge, and fluids; see C. H. Scholz, *Geology* **15**, 493 (1987); S. Cox and C. H. Scholz, *J. Struct. Geol.* **10**, 413 (1988); and C. B. Forster and J. P. Evans, *Geophys. Res. Lett.* **18**, 979 (1991). Since the spacing of grid nodes used in our tomographic inversion is 4 to 5 km, the Kobe earthquake fault zone was imaged as a low-velocity zone not narrower than 4 km.
11. N. Hirata *et al.*, *Proc. 1996 Japan Earth Planet. Sci. Meet.*, 38 (1996); N. Tsumura *et al.*, *ibid.*, p. 39.
12. R. J. O'Connell and B. Budiansky, *J. Geophys. Res.* **79**, 5412 (1974); M. N. Toksoz, C. H. Cheng, A. Timur, *Geophysics* **41**, 621 (1976); D. Moos and M. D. Zoback, *J. Geophys. Res.* **88**, 2345 (1983).
13. To make a checkerboard, we assigned positive and negative velocity anomalies to the 3D grid nodes. Synthetic data are calculated for the checkerboard model. Then we added random errors of 0.05 to 0.15 s to the synthetic data and inverted them with the same algorithm as we did for the observed data. The inverted image of the checkerboard suggests where the resolution is good and where it is poor.
14. Y. Mamada *et al.*, *Progr. Abstr. Fall Meet. Seismol. Soc. Japan*, P37 (1995).
15. E. Fukuyama, *ibid.*, p. A87; K. Tadokoro, Y. Umeda, M. Ando, *Proc. 1996 Japan Earth Planet. Sci. Meet.*, 44 (1996). The direction of the fastest *S* waves is generally oriented east-west in the Nojima fault zone. The time difference between the two splitting *S* waves is generally 0.1 s and does not exceed 0.15 s. This means that the effect of *S*-wave splitting on the accuracy of *S*-wave arrival-time data is not larger than 0.15 s.
16. K. Ito, Y. Umeda, S. Ohmi, A. Ohigashi, K. Matsumura, *Progr. Abstr. Fall Meet. Seismol. Soc. Japan*, A79 (1995).
17. Y. Umeda, T. Yamashita, K. Ito, H. Horikawa, *ibid.*, p. A78.
18. H. Katao, N. Maeda, Y. Hiramatsu, Y. Iio, S. Nakao, *ibid.*, p. A74.
19. K. Obara *et al.*, *Proc. 1996 Japan Earth Planet. Sci. Meet.*, 46 (1996); S. Matsumoto *et al.*, *ibid.*, p. 46.
20. S. N. Chatterjee, A. M. Pitt, H. M. Iyer, *J. Volcanol. Geotherm. Res.* **26**, 213 (1985); M. C. Walck, *J. Geophys. Res.* **93**, 2047 (1988); A. Hasegawa and D. Zhao, in *Magmatic Systems*, M. P. Ryan, Ed. (Academic Press, San Diego, 1994), pp. 179–195.
21. I. Yokoyama, S. Aramaki, K. Nakamura, *Volcanoes* (Iwanami Press, Tokyo, 1987).
22. Y. Okubo, H. Tsu, K. Ogawa, *Tectonophysics* **159**, 279 (1989).
23. R. Kerrich, T. E. La Tour, L. Willmore, *J. Geophys. Res.* **89**, 4331 (1984). Fluids may exist in the middle to lower crust in fault zone environments.
24. K. Hirahara, *Tectonophysics* **79**, 1 (1981); D. Zhao, A. Hasegawa, H. Kanamori, *J. Geophys. Res.* **99**, 22313 (1994).
25. R. H. Sibson, in *Earthquake Prediction: An International Review, Maurice Ewing Ser.*, vol. 4, D. W. Simpson, P. G. Richards, Eds. (American Geophysical Union, Washington, DC, 1981), pp. 593–603; R. H. Sibson, *Tectonophysics* **211**, 283 (1992); S. Hickman, R. H. Sibson, R. Bruhn, *J. Geophys. Res.* **100**, 12831 (1995).
26. We are grateful to the members of the Urgent Observation Group for the 1995 Hyogo-Ken Nanbu Earthquake, who operated the portable stations and picked the *P*- and *S*-wave arrival times, and to the staff members of the seismic networks of Kyoto University, Nagoya University, Kochi University, Kyushu University, and the University of Tokyo for providing the data recorded by their permanent networks that were used in this study. J. Vidale and an anonymous referee provided thoughtful reviews, which improved the manuscript. This work was partially supported by a grant from the National Science Foundation (EAR-9526810) to D. Zhao. This paper is Contribution 5785, Division of Geological and Planetary Sciences, California Institute of Technology.

4 September 1996; accepted 19 November 1996

Paleontology and Chronology of Two Evolutionary Transitions by Hybridization in the Bahamian Land Snail *Cerion*

Glenn A. Goodfriend and Stephen Jay Gould

The late Quaternary fossil record of the Bahamian land snail *Cerion* on Great Inagua documents two transitions apparently resulting from hybridization. In the first, a localized modern population represents the hybrid descendants of a 13,000-year-old fossil form from the same area, introgressed with the modern form now characteristic of the adjacent regions. In the second case, a chronocline spanning 15,000 to 20,000 years and expressing the transition of an extinct fossil form to the modern form found on the south coast was documented by morphometry of fossils dated by amino acid racemization and radiocarbon. Hybrid intermediates persisted for many thousands of years.

Most evolutionary transitions between species are trapped in a no man's land of invisibility. Such events generally require too much time for direct observation but occupy too short an interval for preservation in the fossil record. However, favorable circumstances can provide visibility in fortunate instances. We report two cases of radiometrically dated evolution during the past 20,000 years in the land snail *Cerion*, an exceptionally labile genus that produced several stable and novel populations by the rapid mechanism of hybridization (*1*).

Our perspective on the evolution of hybrid zones has generally been based on either (i) very short periods of human observation, typically related to species introductions or habitat disturbance by humans (2) or (ii) scenarios inferred from knowledge of climatic changes and their probable role in bringing different populations into contact [for example, probable postglacial origins of hybrid zones in fire-bellied toads (*3*) or grasshoppers (*4*)]. In the present study, by contrast, we provide direct fossil evidence for the history of older and more persistent hybrid zones.

Great Inagua (Fig. 1), the largest island of the southeastern Bahamas, is now inhab-

G. A. Goodfriend, Geophysical Laboratory, Carnegie Institution of Washington, 5251 Broad Branch Road, NW, Washington, DC 20015, USA.
S. J. Gould, Museum of Comparative Zoology, Harvard University, Cambridge, MA 02138, USA.

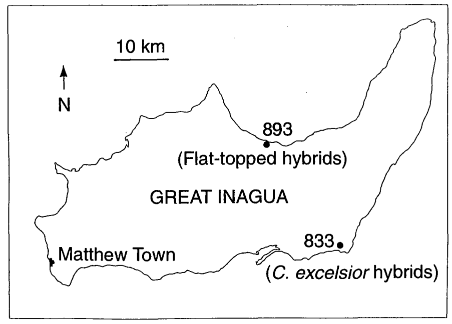

Fig. 1. Map of Great Inagua, showing location of sampling sites.